Performance of long-wave infrared band of microstructured heavily doped InAsSb on type II superlattice layer part 1: the photonic study

Clément Gureghian, Jean-Baptiste Rodriguez, Christophe Dupuis, Nathalie Bardou, Laurence Ferlazzo, Isabelle Ribet, Fernando Gonzalez-Posada, Thierry Taliercio, Grégory Vincent

▶ **To cite this version:**

Clément Gureghian, Jean-Baptiste Rodriguez, Christophe Dupuis, Nathalie Bardou, Laurence Ferlazzo, et al.. Performance of long-wave infrared band of microstructured heavily doped InAsSb on type II superlattice layer part 1: the photonic study. Optics Express, 2024, 32 (8), pp.13438-13449. 10.1364/oe.516043 . hal-04569013

HAL Id: hal-04569013
https://hal.science/hal-04569013

Submitted on 6 May 2024

HAL is a multi-disciplinary open access archive for the deposit and dissemination of scientific research documents, whether they are published or not. The documents may come from teaching and research institutions in France or abroad, or from public or private research centers.

L'archive ouverte pluridisciplinaire **HAL**, est destinée au dépôt et à la diffusion de documents scientifiques de niveau recherche, publiés ou non, émanant des établissements d'enseignement et de recherche français ou étrangers, des laboratoires publics ou privés.

Copyright

Research Article | Vol. 32, No. 8 / 8 Apr 2024 / Optics Express 13438
Optics EXPRESS

Performance of long-wave infrared band of microstructured heavily doped InAsSb on type II superlattice layer part 1: the photonic study

CLÉMENT GUREGHIAN,[1] JEAN-BAPTISTE RODRIGUEZ,[2] CHRISTOPHE DUPUIS,[3] NATHALIE BARDOU,[3] LAURENCE FERLAZZO,[3] ISABELLE RIBET,[1] FERNANDO GONZALEZ-POSADA,[2] THIERRY TALIERCIO,[2,4] AND GRÉGORY VINCENT[2,5]

[1]*ONERA - The French Aerospace Lab, Paris-Saclay University, Palaiseau, 91123, France*
[2]*Institut d'Electronique et des Systemes (IES), University of Montpellier, Montpellier, 34095, France*
[3]*Centre de Nanosciences et de Nanotechnologies (C2N), CNRS, Paris-Saclay University, Palaiseau, 91120, France*
[4]*thierry.taliercio@umontpellier.fr*
[5]*gregory.vincent@onera.fr*

Abstract: This article deals with the optical study of nanostructured components which absorb light across the entire long-wave infrared (LWIR) spectral band. The components are made of type-II superlattice (T2SL) absorber and highly doped InAsSb, the latter being nanostructured to ensure multiple resonances. We studied two components: in the first one, the T2SL has a thickness of 1.6 μm, and in the second its thickness is 300 nm. The calculated absorption spectra were shown and the components revealed high absorption thanks to optical resonance and high angular acceptance. A fabrication process has been developed, and optical measurements have confirmed the reliability of the model.

© 2024 Optica Publishing Group under the terms of the Optica Open Access Publishing Agreement

1. Introduction

The nanostructuring of photodetectors has been proposed for more than fifteen years as a means of improving their performance or to embed optical functions with high compacity [1]. This has been made possible thanks to the capacity of nanoresonators or photonic crystals to confine light in small volumes [2–5], to shape wavefronts, or to polarize light [6–10]. This strategy has been derived over a wide photodetection spectral range and range of materials, such as visible light and short-, mid-, and long-wave infrared (SWIR, MWIR and LWIR), presenting various challenges. As an example, polarizing image sensors can thus be produced using lamellar metallic gratings whose orientation varies according to the focal plane array, thereby selecting the polarization orientation [11]. Other optical features can be envisaged with metallic or dielectric structures, such as wavefront control [12,13]. These last examples involve metasurfaces which can be deposited on standard photodetectors with usual thicknesses. Conversely, semiconductors can be part of the metasurface, in order to benefit from field enhancement in small volumes. New-generation solar cells can advantageously use resonant nanostructures in order to reduce material consumption with no drop in efficiency [14]. For slightly longer wavelengths, light-matter coupling strategies involving nanostructures have also been proposed for SWIR photodetection with colloidal quantum dots (CQD). The nanopatterning of electrodes allows enhanced absorption in the thin CQD film at the resonance wavelength of the nanostructures, and better charge collection, which leads to improved detectivity [15]. Also, in the MWIR and LWIR spectral range, for bulk or super-lattice semiconductors, metallic nanostructures are deposited on a thin epitaxial layer in order to develop multispectral arrays and/or to lower the dark current, maintaining reasonable quantum efficiency at specific wavelengths [16–23]. However, the previously cited works (except

#516043 https://doi.org/10.1364/OE.516043
Journal © 2024 Received 15 Dec 2023; revised 9 Feb 2024; accepted 11 Feb 2024; published 27 Mar 2024

Optics EXPRESS

on CQD) require sample transferring on a holding wafer, and the etching of the epitaxial substrate. This leads to non-trivial chemical processes that can damage the active region. To avoid this, lattice-matched highly doped semiconductors can be chosen instead of the metals traditionally used for plasmonics, for example n^{++}-InAsSb:Si [24–27]. Wasserman's group proposed to grow thin MWIR or LWIR photodetectors on an n^{++}-InAsSb:Si mirror and capped with a metallic or semiconductor pattern [28–35]. In particular, Refs. [31] and [32] show wide-band nanostructured photodetectors based on an nBn stack, whose dark current is below "Rule 07" curve for operating temperatures of 90K to 230K. Two of these references ([28] and [30]) present the study of angular acceptance in one incidence plane. In particular, guided-mode resonance studied in Ref. [30] shows low angular acceptance, which could be prohibitive for imaging applications.

In this article we present the optical part of the study, over a wide LWIR spectral range (8-12 μm), of two stacks made of an n^{++}-InAsSb:Si mirror, a thin Type 2 super-lattice (T2SL) photodetector, and an n^{++}-InAsSb:Si pattern. First, we describe the expected performance through simulations: we present the calculations of total absorption spectra on the one hand, and absorption in the T2SL layer on the other. We consider that the latter can be assimilated to a maximum external quantum efficiency. We then present an experimental study based on reflectivity measurements. In particular, we see that the etching profile of the gratings and its etching depth have a strong influence on the absorption spectra of the components.

2. Device design

The samples are "metal-free" devices exclusively based on semiconductors. Our goal was to set geometrical parameters so that the absorption is maximized within the T2SL layer, in the LWIR range. Both devices were made of a $1\mu m$-thick n^{++}-InAsSb:Si mirror, a $100nm$ or $200nm$ GaSb layer, a T2SL layer and, lastly, a patterned n^{++}-InAsSb:Si layer. They differed in their thicknesses and patterning. The thicknesses of the T2SL and capping n^{++}-InAsSb:Si layers would be either $300nm$ and $500nm$, respectively, for the thin component, or $1.6\mu m$ and $1.5\mu m$ for the thick component. To reduce the calculation time during the design process, the capping layer would be structured according to a 1D pattern, (see Fig. 1). The T2SL thicknesses with microstructured surface should be compared with standard T2SL thicknesses, which are usually a few microns thick (see 3.2 for comparison).

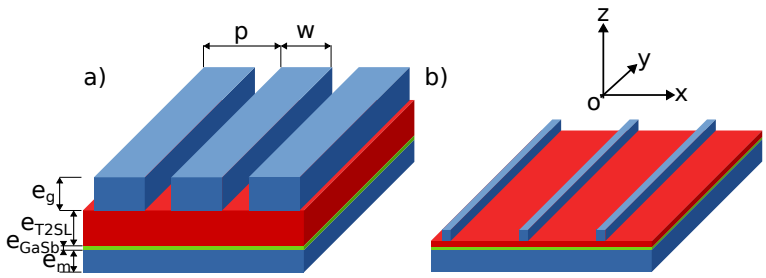

Fig. 1. Blue: n^{++}-InAsSb:Si. Green: *GaSb*. Red: *T2SL*. a) Thick structure: $p = 3.5\mu m$, $w = 2.3\mu m$, $e_g = 1.5\mu m$, $e_{T2SL} = 1.6\mu m$, $e_{GaSb} = 0.2\mu m$, $e_m = 1\mu m$. b) Thin structure: $p = 3.5\mu m$, $w = 0.4\mu m$, $e_g = 0.5\mu m$, $e_{T2SL} = 0.3\mu m$, $e_{GaSb} = 0.1\mu m$, $e_m = 1\mu m$

3. Numerical study

We present the absorption spectra under different polarizations and angles of incidence. The total absorption corresponds to the contribution of the T2SL and all the metallic layers (n^{++}-InAsSb:Si) of the devices. We extract the absorption in the T2SL: this represents the maximum value for quantum efficiency, which will have to be assessed by optoelectronic measurements. The T2SL

Optics EXPRESS

thickness should be compared to the vertical diffusion length of carriers, which is found to be more than micrometer, as previously shown on an intrinsic region of a weakly p doped p-i-n photodiode, with unintentionally i and n doped regions [36–38].

The permittivity of n^{++}-InAsSb:Si is described by a Drude model. The parameters ϵ_∞, γ and ω_p correspond to the dynamic dielectric permittivity, the scattering rate, and the screened plasma frequency respectively. For ϵ_∞ and γ, values are taken from Ref. [39], where they were determined with a fit with experimental data at different temperatures. The screened plasma frequency ω_p was experimentally determined by measuring the Brewster mode [40].

$$\epsilon(\omega) = \epsilon_\infty(1 - \frac{\omega_p^2}{\omega(\omega + i\gamma)}) \tag{1}$$

In the present article, all measurements would be done at $T = 300K$, so we take $\epsilon_\infty = 10.4$, $\gamma = 2 \cdot 10^{13} rad \cdot s^{-1}$, and $\omega_p = 3.74 \cdot 10^{14} rad \cdot s^{-1}$ for $N = 6.2 \cdot 10^{19} cm^{-3}$.

The refractive index of GaSb is $n_{GaSb} = 3.7$ [41]. For the T2SL layer, the refractive index is chosen to be constant, so that the cut-off frequency of the material does not influence the design. From [42], we take the absorption coefficient $\alpha \approx 1400 cm^{-1}$ for $\lambda = 9\mu m$ (away from cut-off), which leads to the imaginary part of the refractive index $\kappa \approx 0.1$ ($\alpha = \frac{4\pi\kappa}{\lambda}$). The real part $n \approx 3.7$ is extrapolated from MWIR measurements where it is found to be almost constant far from the cut-off [43]. Note that the imaginary part of the permittivity is anisotropic, as a consequence of the polarisation selectivity rule for the absorption in T2SL ([44]). As a fairly strong approximation, we have considered that its component along the z axis equals zero. Calculations are achieved using COMSOL Multiphysics software, with RF Module.

3.1. Normal incidence

At the top of Fig. 2(a) and (b), we show the calculated absorption spectra, under normal incidence, for transverse magnetic (TM - $\overrightarrow{H}$ along $\overrightarrow{y}$ axis) and transverse electric (TE - $\overrightarrow{E}$ along $\overrightarrow{y}$ axis) polarization for thick (a) and thin (b) structures. At the bottom of this figure, we also give the absorption of stacks with or without unpatterned n^{++}-InAsSb:Si cap layer.

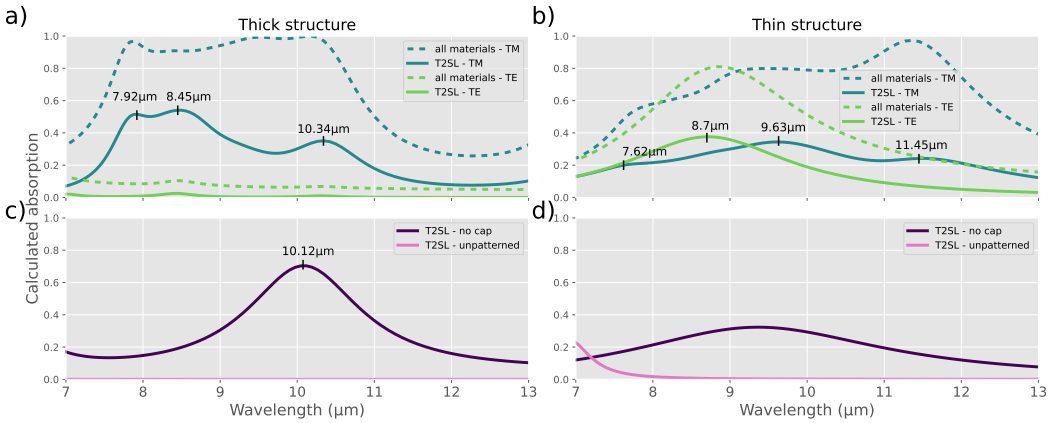

Fig. 2. Calculated absorption spectra under normal incidence. Plain curve: absorption in T2SL layer. Dashed curve: absorption in all materials. Total absorption reaches a value of 1. a-c) Thick stack . b-d) Thin stack.

Stacks without cap layer (purple curves) lead to single Fabry-Perot resonances in the LWIR range, which can lead to high absorption, in relation to the T2SL thicknesses at a specific wavelength (71% for 1.6μm-thick T2SL and 32% for 0.3μm-thick T2SL). The unpatterned cap layer reflects all the light in the spectral region of interest.

Optics EXPRESS

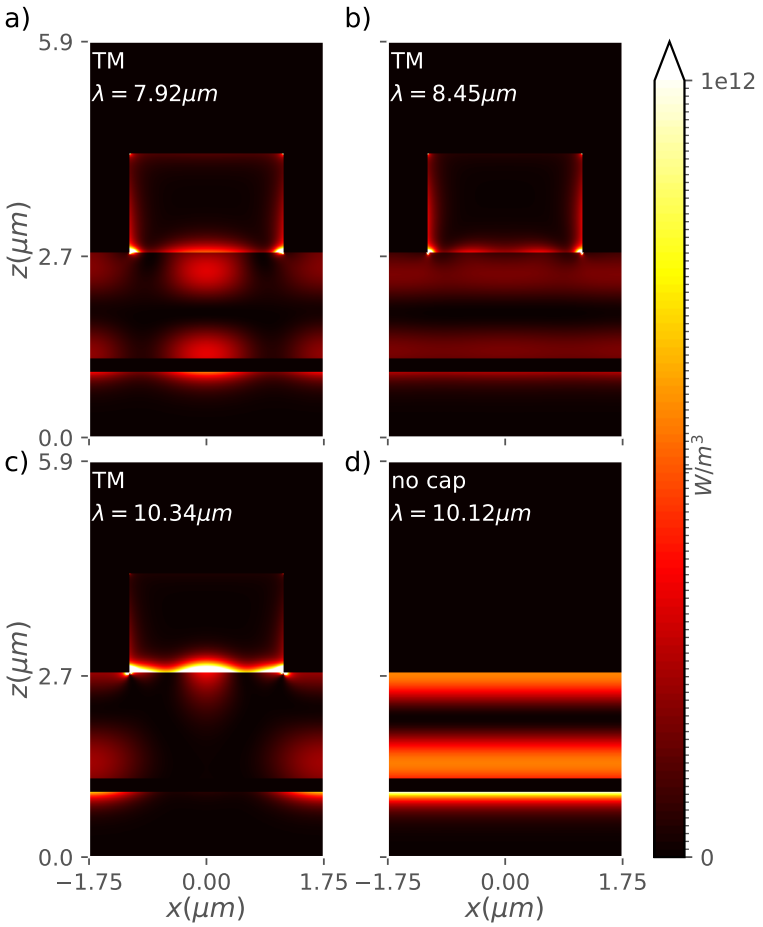

Fig. 3. The calculated absorption maps, under normal incidence and TM polarization, for various wavelengths. The colorbar has an upper limit of $10^{12} W/m^3$ so that the hotspot does not hide absorption. a) Patterned thick structure, TM polarization, $\lambda = 7.92\mu m$. b) Patterned thick structure, TM polarization, $\lambda = 8.45\mu m$. c) Patterned thick structure, TM polarization, $\lambda = 10.34\mu m$. d) Thick structure without InAsSb cap, $\lambda = 10.12\mu m$.

Conversely, stacks with nanostructured capping layer shows absorption spectra with multiple resonances across the entire LWIR range, for TM polarization (see blue curves in 2). Although the absorption in all materials of the components (*i.e.* absorption in InAsSb and T2SL layers, see dashed blue curves) can be very high, only part of this could generate photocurrent (see plain blue curves, the absorption in T2SL). Moreover, the absorption in T2SL can reach up to 54% ($\lambda = 8.45\mu m$) for the thick structure, and 35% ($\lambda = 9.63\mu m$) for the thin structure, compared to the uncapped T2SL layers. TE polarization (green curves) shows negligible absorption for the thick structure and 37% with single resonance absorption for the thin structure. Interestingly, the absorption in 2(b) doubles at $11.45\mu m$ due to the patterned n^{++}-InAsSb:Si cap layer.

Figure 3 shows absorption vertical stack profiles at selected resonant wavelengths for the thick structure, for TM polarization, with an InAsSb patterning (Fig. 3(a)), Fig. 3(b)), Fig. 3(c))) or with no InAsSb cap (Fig. 3(d))). As expected from the spectra of Fig. 2(c)), the absorption map of Fig. 3(d)) reveals vertical Fabry-Perot resonance in the T2SL layer. Such resonance is also visible in Fig. 3(b)), slightly perturbed by InAsSb. Figure 3(a)) shows a horizontal pattern, which

Optics EXPRESS

means that the wavevector of the resonant mode has a horizontal component. This could be due to the diffraction of the grating and is compatible with the existence condition of guided-mode resonance in the T2SL layer [45]. In both Fig. 3(a)) and 3(b), an intense (slight) absorption enhancement at the lower (upper) corners of the patterned InAsSb cap layer points to the localized surface plasmonic behavior of the patterned stacks. Conversely, Fig. 3(c)) shows absorption at the interface of the T2SL and InAsSb layer, which suggests the involvement of a horizontal higher-order surface plasmon. In the latter case, a particularly high amount of absorption also occurs in InAsSb, which is confirmed by Fig. 2(a)).

Figure 4 shows absorption maps at selected resonant wavelengths for the thin structure, for TM or TE polarization. Figures 4(a)) and c) show field enhancement at the InAsSb interface with the T2SL layer, for a TM polarized wave, which indicates that localized surface plasmons are involved, in relation to the absorption curves in Fig. 2(b)) at $7.62\mu m$ and $11.45\mu m$. Conversely, the absorption maps in Figs. 4(b)) and d) show that absorption also occurs in the T2SL layer away from InAsSb, and the field distribution suggests vertical Fabry-Perot-like resonances, slightly perturbed by InAsSb.

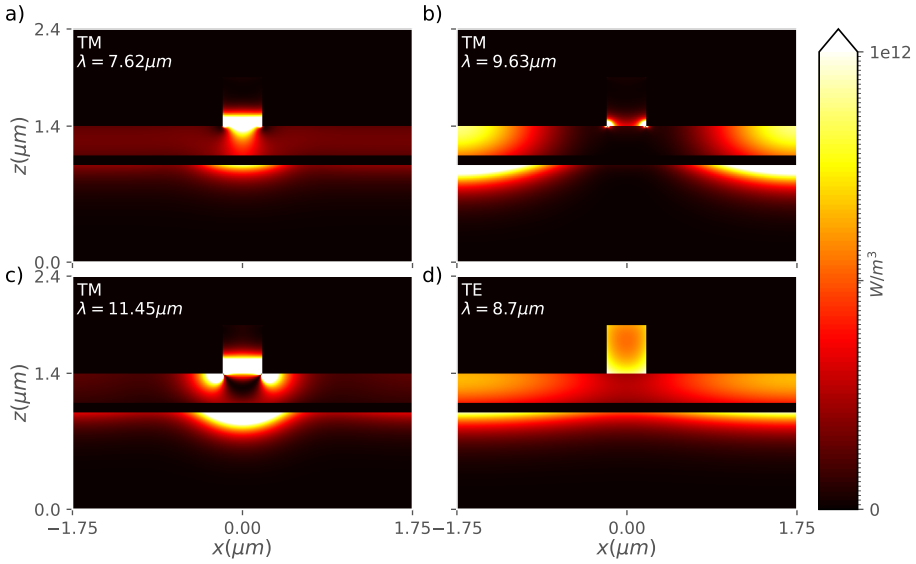

Fig. 4. Calculated absorption maps for the thin structure, under normal incidence and TM or TE polarization, for various wavelengths. The colorbar has an upper limit of $1e12W/m^3$ so that hotspot does not hide absorption. a) TM polarization, $\lambda = 7.62\mu m$. b) TM polarization, $\lambda = 9.63\mu m$. c) TM polarization, $\lambda = 11.45\mu m$. d) TE polarization, $\lambda = 8.7\mu m$.

3.2. *Comparison with standard T2SL*

In the previous section, we presented selected geometries of components for wide-band absorption over the whole LWIR spectral range. The total absorption is high, combining low absorption in a very thin T2SL thanks to a patterned cap layer. For the sake of comparison with a standard T2SL layer without optical resonance, we can calculate the thickness e_{T2SL}^{stand} required to absorb the same amount of photons as our structures. We will assume that the standard T2SL would have a perfect anti-reflective coating and double-pass optical path thanks to a back mirror, similar to the n^{++}-InAsSb:Si mirror layer.

Without optical resonance, intensity decreases following the Beer-Lambert's law $I(z) = I_0 e^{-\frac{4\pi\kappa}{\lambda}z}$, where $I_0 = 1$ is assumed thanks to an anti-reflective coating. We find that $e_{T2SL}^{stand} \approx 2.65\mu m$

Optics EXPRESS

is necessary to reach 54% of absorption at $\lambda = 8.45\mu m$, and $e_{T2SL}^{stand} \approx 1.5\mu m$ is necessary to reach 35% of absorption at $\lambda = 9.63\mu m$. These values represent approximately a factor of $\times 1.65$ and $\times 5$ of thicknesses for our thick ($1.6\mu m$) and thin ($0.3\mu m$) structures.

3.3. Influence of the angle of incidence

In this section, we will see the influence of the angle of incidence on the absorption spectra of the components. This property is of great interest for the design of imaging systems, where standard apertures typically involve angles of incidence of up to 25°. The angle of incidence is here defined in the half space with two angles θ and δ. Figure 5(a)) and Fig. 5(b)) show dispersion diagrams for absorption in the T2SL layer for thick and thin stacks, respectively, where the angle of incidence θ varies between 0° and 60° in the incidence plane $x0z$. Absorption in the active layer is given in linear colorscale. We can see high stability of the resonances, at least up to 50°.

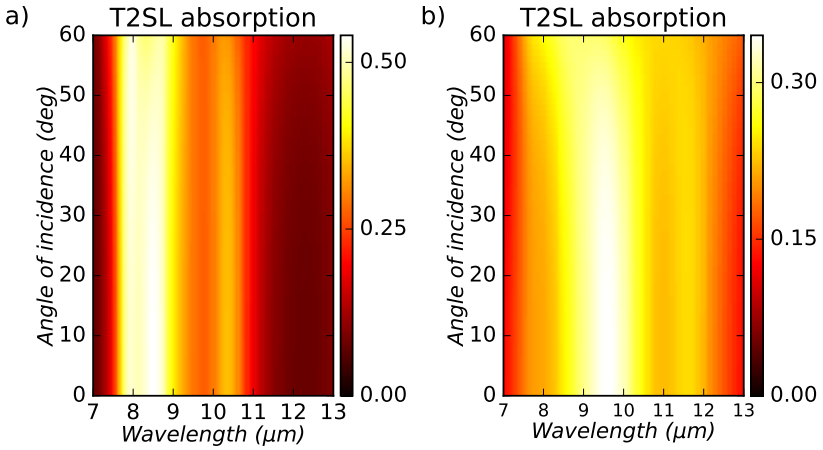

Fig. 5. Calculated dispersion diagrams for absorption in T2SL layer, under TM polarized wave, for an angle of incidence ranging from 0° to 60° in the $x0z$ plane. a) Thick structure ; b) thin structure.

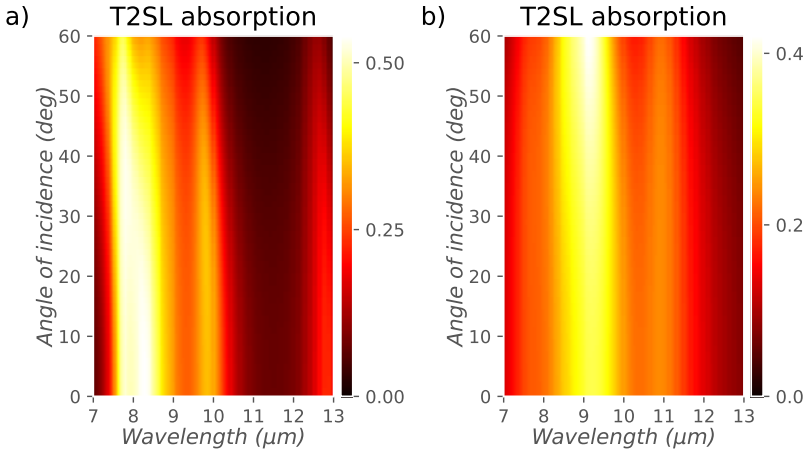

Fig. 6. Calculated dispersion diagrams for absorption in T2SL layer, under TM polarized wave, for an angle of incidence ranging from 0° to 60° in the $y0z$ plane. a) Thick structure ; b) thin structure.

Optics EXPRESS

In Fig. 6, for angles δ in the $y0z$ plane, high stability is also apparent. These results confirm that components can retain their spectral properties even when integrated into imaging systems, with a focused beam.

4. Experimental study

In this section, we will present the experimental study of the components. We remind the reader that, in this article, we focus only on optical study. We proceeded with reflectivity measurements using a microscope objective coupled with a Fourier transform infrared (FTIR) spectrometer and deduced the total absorption, as there is no transmission through the component.

4.1. Fabrication process

As depicted in Fig. 1, the samples consisted of T2SL embedded between two layers of n^{++}-InAsSb:Si. The samples were grown on n-doped ($1-2\cdot10^{18}cm^{-3}$) GaSb substrates using a RIBER-C21 solid source molecular beam epitaxy tool. Prior to the growth, thermal desorption is performed to remove the native oxide. First, a $210nm$ thick buffer layer of undoped GaSb is grown in order to smooth out the surface and to burry any remaining impurities left after deoxidation. A $1\mu m$ thick n^{++}-InAsSb:Si layer is then grown. The layer is grown as a digital alloy, *i.e.* a very short period superlattice, with an estimated doping level of $6.2\cdot10^{19}cm^{-3}$. A p-doped GaSb:Si layer of $200nm$ or $100nm$ is then grown prior to the deposition of the *p-i-n* junction based T2SL. The semi-metallic interface formed between the InAsSb n and GaSb p layers allows electrons to transfer the photo-current flowing out of the p-type T2SL into the n-type lower part of the structure formed by the InAsSb contact layer. The T2SL is a 14/7 MLs InAs/GaSb SL. The *p-i-n* T2SL junction consists of a p-doped ($10^{18}cm^{-3}$) InAs/GaSb SL layer, a non-intentionally doped InAs/GaSb SL active region and a n-doped ($10^{18}cm^{-3}$) InAs/GaSb layer. Thicknesses are $100nm/1.4\mu m/100nm$ or $25nm/250nm/25nm$ for thick or thin structures, respectively. Finally, an n^{++}-InAsSb:Si, of $1.5\mu m$ or $0.5\mu m$ thickness for thick or thin structures respectively, completes the samples.

On this stack, the microstructures were fabricated using a new process development. Series AZ nLOF 500nm-grade negative resists were used to design the patterns and employed as an etching mask. The electron sensitivity of this resist allowed us to obtain high-resolution using e-beam lithography with a low energy ($70\mu C/cm^2$), provided by an industrial Vistec5000+ ebeam system and using a 0.26N (2.38%) TMAH for resist development. High vertical patterns were obtained and transferred in the InAsSb layer using ICP-RIE Sentech equipment. This new process has been developed to obtain high anisotropy and good selectivity versus the resist mask. This study has led to an optimized process using a 30 sccm HBr and 1 sccm O_2 gas mixture at low pressure and high temperature (150°C), showing very anisotropic patterns thanks to controlled SiO_xBr_y passivation deposition on the sidewall. The bottom and sidewall displayed a very smooth aspect. An original study was carried out on the influence on the etched profile of the orientation of the patterns on the wafer and particularly the impact of this orientation versus the flat. This parameter was shown to have a strong effect on the anisotropy of the patterns. When the patterns were perpendicular to the flat, a high anisotropic profile was obtained. Conversely, when the patterns were parallel to the flat, anisotropy decreased, leading to slopes on the profile.

Figures 7(a))-c) shows scanning electron microscope (SEM) images of the sample for the thick structure. Various geometries and orientations were fabricated on the same sample, over an area of $100\mu m$x$100\mu m$ for each pattern (Fig. 7(a))). The width of the ribbon is either $w = 2350nm$ (labeled $A1$ or $B1$), $w = 2300nm$ ($A2$ or $B2$), or $w = 2250nm$ ($A3$ or $B3$). The patterns were oriented at 0° or 90° vis-a-vis the crystal plane for patterns A and B, respectively. Figures 7(b)) and c) show zooms at the bottom of a ribbon, which reveal a different etching profile depending on the orientation. In particular, we see in Fig. 7(b)) an etching profile with a triangular base

Optics EXPRESS

as depicted in Fig. 7(d)). Figure 7(c)) shows a vertical profile, but measurements show that the InAsSb layer has not been etched to its full thickness, and a thickness of $C_e \approx 380nm$ (see Fig. 7(e))) remains.

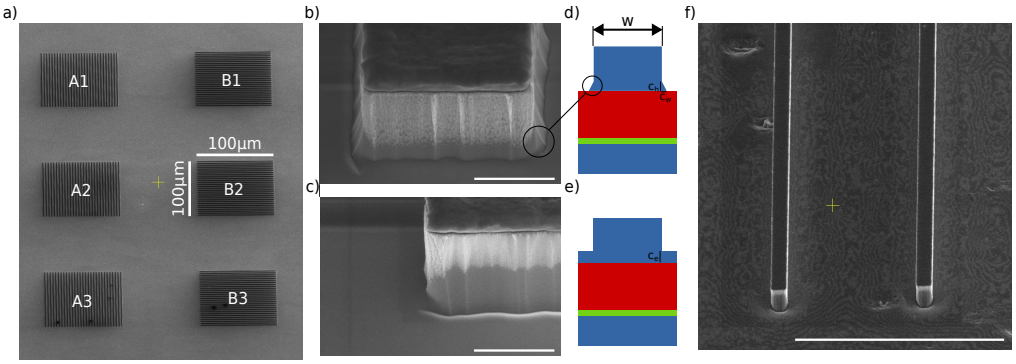

Fig. 7. a) Overview of samples. A-labelled and B-labelled patterns are oriented 0° and 90° vis-a-vis the crystal plane, respectively. b) Scale bar: $1\mu m$. Zoom on a thick ribbon, revealing a triangular base, illustrated in d). c) Scale bar: $1\mu m$. Other side view of a thick ribbon : vertical etching is revealed. e) Scale bar : $5\mu m$. Thin ribbon.

In the next paragraphs, we see the consequences of these real geometries on the absorption spectra. We proceed to consider the reflectivity measurements under TM polarization and we compare the results to the calculations.

4.2. Reflectivity measurements

Reflectivity measurements were made using a Bruker Hyperion microscope coupled with an FTIR spectrometer. The Schwarzschild microscope objective involves an angle of incidence from 12° to 24°. As we have seen in Figs. 5 and 6, the absorption spectra are barely different in this angular range. Consequently, reflectivity measurements are compared to calculations made under plane wave at normal incidence.

4.2.1. Thick structure

In Fig. 8(a)), we compare the absorption spectra of a thick structure for the three geometrical variations and two orientations. On the one hand, we can see that compared to the structure initially designed (Fig. 8(b)) red curve), resonance at $\lambda \approx 10\mu m$ vanishes and only two peaks around $\lambda = 8\mu m$ remain. This is due to a remaining unstructured InAsSb layer above T2SL, because the etching time was too short. This is confirmed by the model whose calculated absorption is presented in Fig. 8(b)) (green curve). It shows that a thin un-etched InAsSb layer kills the high wavelength resonance ($C_e = 380nm$).

Moreover, Fig. 8(a)) also shows that a triangle-based etching profile decreases the value of absorption (green curves versus blue curves) but does not shift the resonance wavelengths, which tends to prove that these are vertical resonances. This is confirmed by calculations in Fig. 8(b)) (blue curve), where the model involves both unstructured InAsSb layer ($C_e = 380nm$) and triangle-based etch profile ($C_w = 170nm$ and $C_h = 200nm$) .

Lastly, measured and calculated absorption peaks do not occur at strictly the same wavelengths. Because the thicknesses are well known due to the epitaxial process, these shifts were attributed to a lack of knowledge of the T2SL and GaSb refractive indices.

Optics EXPRESS

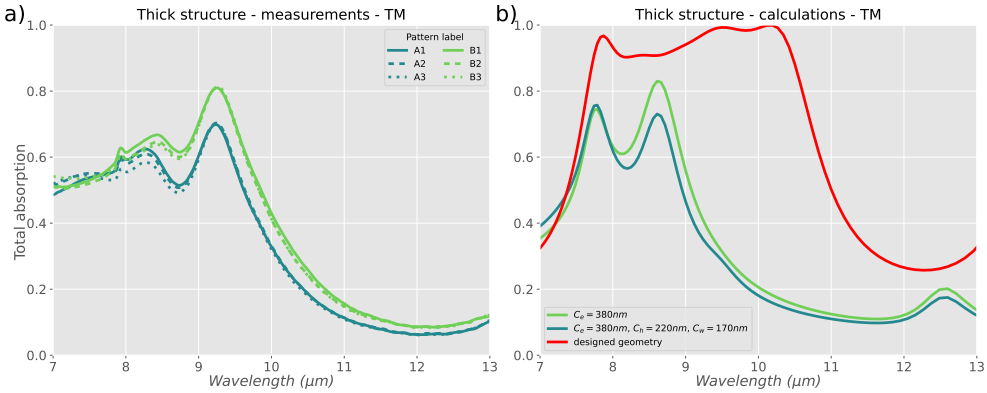

Fig. 8. a) Measured absorption spectra for various geometries. Green : w = 2350nm/2300nm/2250nm. For the pattern label, see Fig. 7. Blue : same geometries as green but with triangle-based profile. b) Calculated absorption spectra for various geometries. Red: standard etching profile. Green and blue: see geometrical parameters in legend, with w = 2300nm.

4.2.2. Thin structure

Regarding the thin structure, measurements show, as expected, a wide-band absorption spectra for every geometrical variation (Fig. 9(a))). Measurements for the two orientations (green and blue curves) show that the etching profile has a strong influence on the absorption spectra, and we see a shift of the high wavelength resonance to a higher wavelength for structures with an enlarged base, as expected from the plasmonic behavior of the microstructured cap layer.

Figures 9(b))-d) show the influence of geometrical parameters on the absorption spectra. In Fig. 9(b)), we see a red shift of the high wavelength resonance with w, for an ideal vertically etched grating. This observation is consistent with the measurements. In Figs. 9(c)), we evaluate the influence of geometry with a triangular base (Fig. 7(d))). Both parameters C_w and C_h have an influence on the high wavelength resonance. C_w enlarges the bottom of the grating, which shifts the resonance towards a higher wavelength. The C_h parameter has the opposite effect. Under-etching is the last geometrical parameter that was studied, shown in Fig. 9(d)). In a similar way to the thick component, a thin remaining unstructured InAsSb layer (Fig. 7(e))) kills and blue-shifts the high wavelength resonance. Because this resonance is clearly visible on the measurements, we deduce that the etching time was sufficient.

In Fig. 9(e)), we adjust the geometries so that we have a better fit with the measurements. In particular, the blue curves have a triangular base with C_h = 150nm and C_w = 50nm. The peak positions are quite similar, but we see some discrepancies in the absorption maxima for high-wavelength resonances. The values are overestimated in the calculations, which may be due to a lack of knowledge of the T2SL refractive index, which is here kept constant. In particular, the cut-off of the T2SL layer is not known with high accuracy, but it is probably in the 11μm-12μm spectral range.

Optics EXPRESS

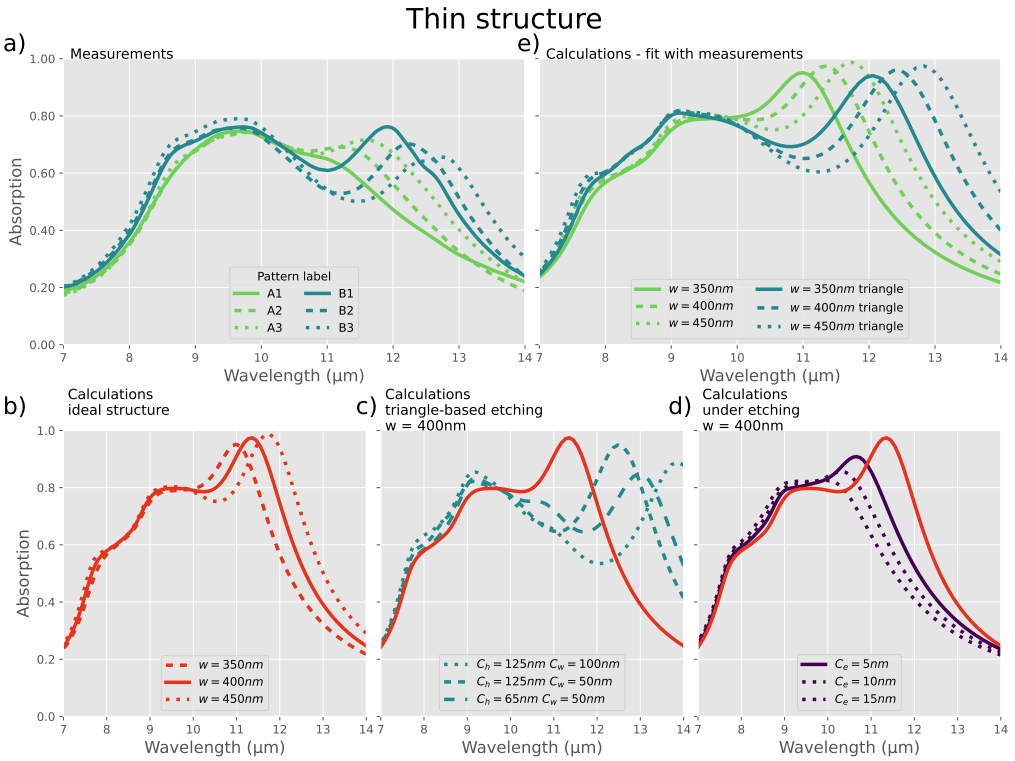

Fig. 9. Incoming wave has TM polarization. a) Measurements for different geometrical variations and orientation of thin structure. b) Calculated absorption, for ideal binary structure for various values of w. c) Calculated absorption for various triangular based geometries. d) Calculated absorption with under-etching. e) Calculations with geometrical parameters adjusted for the best fit with measurements.

5. Conclusion

In this article, we have designed and measured absorbing structures over the full LWIR band, made up of thin T2SL, highly-doped InAsSb mirror and highly-doped InAsSb grating. The components revealed high angular acceptance, which makes them compatible with integration in an imaging system. Experimental data has shown that particular care must be taken during the etching process to avoid a remaining unstructured InAsSb layer, because this has a strong influence on the optical response. Otherwise, we could guess that over-etching would also have a strong influence on the electronic properties and might significantly decrease performance. This is the reason why we would suggest, for future experiments, adding an etch-stop layer in the stack. Furthermore, triangle-base grating has an influence on the absorption spectra. However, this phenomenon is well predicted by calculations and must be taken into account in the design step. Such components can be of interest for reducing the dark current of LWIR photodetectors because, thanks to optical resonances, the thickness of the T2SL layer can be reduced. In addition, we could also expect better charge collection and maybe better epitaxial quality for thin structures, which would tend to enhance the relevance of the use of microstructures. These assumptions are currently under investigation in our laboratories. Finally, integrating this type of structure into an FPA requires the development of a specific fabrication process, which is not covered in this article.

Optics EXPRESS

Funding. Conseil Départemental de l'Essonne; Centre National de la Recherche Scientifique (RENATECH); Agence de l'innovation de Défense (ANR 19-ASTR-0003-01); Agence Nationale de la Recherche (ANR 11-EQPX-0016, EquipEx EXTRA).

Acknowledgements. The authors wish to thank Baptiste Fix from ONERA for contributing to the discussions about reflection measurements and Jean-Paul Hugonin from IOGS for his help on simulations.

Disclosures. The authors declare no conflicts of interest.

Data availability. Data underlying the results presented in this paper are available in Ref. [46].

References

1. P. Martyniuk, J. Antoszewski, M. Martyniuk, *et al.*, "New concepts in infrared photodetector designs," Appl. Phys. Rev. **1**(4), 041102 (2014).
2. R. F. Oulton, V. J. Sorger, D. A. Genov, *et al.*, "A hybrid plasmonic waveguide for subwavelength confinement and long-range propagation," Nat. Photonics **2**(8), 496–500 (2008).
3. A. Cattoni, P. Ghenuche, A.-M. Haghiri-Gosnet, *et al.*, "λ^3 /1000 Plasmonic Nanocavities for Biosensing Fabricated by Soft UV Nanoimprint Lithography," Nano Lett. **11**(9), 3557–3563 (2011).
4. P. Chevalier, P. Bouchon, J.-J. Greffet, *et al.*, "Giant field enhancement in electromagnetic Helmholtz nanoantenna," Phys. Rev. B **90**(19), 195412 (2014).
5. A. Bierret, G. Vincent, J. Jaeck, *et al.*, "Pixel-sized infrared filters for a multispectral focal plane array," Appl. Opt. **57**(3), 391 (2018).
6. Z. Wang, T. Li, A. Soman, *et al.*, "On-chip wavefront shaping with dielectric metasurface," Nat. Commun. **10**(1), 3547 (2019).
7. N. A. Rubin, P. Chevalier, M. Juhl, *et al.*, "Imaging polarimetry through metasurface polarization gratings," Opt. Express **30**(6), 9389 (2022).
8. T. Ellenbogen, K. Seo, and K. B. Crozier, "Chromatic Plasmonic Polarizers for Active Visible Color Filtering and Polarimetry," Nano Lett. **12**(2), 1026–1031 (2012).
9. E. Arbabi, S. M. Kamali, A. Arbabi, *et al.*, "Full-Stokes Imaging Polarimetry Using Dielectric Metasurfaces," ACS Photonics **5**(8), 3132–3140 (2018).
10. G. P. Nordin, J. T. Meier, P. C. Deguzman, *et al.*, "Micropolarizer array for infrared imaging polarimetry," J. Opt. Soc. Am. A **16**(5), 1168 (1999).
11. S. Junger, W. Tschekalinskij, N. Verwaal, *et al.*, "On-chip nanostructures for polarization imaging and multispectral sensing using dedicated layers of modified CMOS processes," (San Francisco, California, 2011), p. 79461D.
12. L. Verslegers, P. B. Catrysse, Z. Yu, *et al.*, "Planar metallic nanoscale slit lenses for angle compensation," Appl. Phys. Lett. **95**(7), 071112 (2009).
13. Z. Li, S. Yu, and G. Zheng, "Advances in exploiting the degrees of freedom in nanostructured metasurface design: from 1 to 3 to more," Nanophotonics **9**(12), 3699–3731 (2020).
14. H.-L. Chen, A. Cattoni, R. De Lépinau, *et al.*, "A 19.9%-efficient ultrathin solar cell based on a 205-nm-thick GaAs absorber and a silver nanostructured back mirror," Nat. Energy **4**(9), 761–767 (2019).
15. Chu Audrey, Martinez Bertille, and Livache Clément, "Near Unity Absorption in Nanocrystal Based Short Wave Infrared Photodetectors Using Guided Mode Resonators," ACS Photonics **6**(10), 2553–2561 (2019).
16. J. Rosenberg, R. V. Shenoi, T. E. Vandervelde, *et al.*, "A multispectral and polarization-selective surface-plasmon resonant midinfrared detector," Appl. Phys. Lett. **95**(16), 161101 (2009).
17. J. Le Perchec, Y. Desieres, and R. Espiau de Lamaestre, "Plasmon-based photosensors comprising a very thin semiconducting region," Appl. Phys. Lett. **94**(18), 181104 (2009).
18. J. A. Nolde, M. Kim, C. S. Kim, *et al.*, "Resonant quantum efficiency enhancement of midwave infrared *nBn* photodetectors using one-dimensional plasmonic gratings," Appl. Phys. Lett. **106**(26), 261109 (2015).
19. E. Jackson, J. Nolde, M. Kim, *et al.*, "Two-dimensional plasmonic grating for increased quantum efficiency in midwave infrared nBn detectors with thin absorbers," Opt. Express **26**(11), 13850–13864 (2018).
20. M. D. Goldflam, E. A. Kadlec, B. V. Olson, *et al.*, "Enhanced infrared detectors using resonant structures combined with thin type-II superlattice absorbers," Appl. Phys. Lett. **109**(25), 251103 (2016).
21. J. Montoya, Z.-B. Tian, S. Krishna, *et al.*, "Ultra-thin infrared metamaterial detector for multicolor imaging applications," Opt. Express **25**(19), 23343–23355 (2017).
22. D. Palaferri, Y. Todorov, A. Bigioli, *et al.*, "Room-temperature nine-μm-wavelength photodetectors and GHz-frequency heterodyne receivers," Nature **556**(7699), 85–88 (2018).
23. H. T. Miyazaki, T. Mano, T. Kasaya, *et al.*, "Synchronously wired infrared antennas for resonant single-quantum-well photodetection up to room temperature," Nat. Commun. **11**(1), 565 (2020).
24. T. Taliercio and P. Biagioni, "Semiconductor infrared plasmonics," Nanophotonics **8**(6), 949–990 (2019).
25. Y. Zhong, S. D. Malagari, T. Hamilton, *et al.*, "Review of mid-infrared plasmonic materials," J. Nanophotonics **9**(1), 093791 (2015).
26. S. Law, L. Yu, and D. Wasserman, "Epitaxial growth of engineered metals for mid-infrared plasmonics," J. Vac. Sci. Technol., B: Nanotechnol. Microelectron.: Mater., Process., Meas., Phenom. **31**(3), 03C121 (2013).
27. V. N'Tsame Guilengui, L. Cerutti, J.-B. Rodriguez, *et al.*, "Localized surface plasmon resonances in highly doped semiconductors nanostructures," Appl. Phys. Lett. **101**(16), 161113 (2012).

Optics EXPRESS

28. S. Wang, N. Yoon, A. Kamboj, *et al.*, "Ultra-thin enhanced-absorption long-wave infrared detectors," Appl. Phys. Lett. **112**(9), 091104 (2018).
29. L. Nordin, A. Kamboj, P. Petluru, *et al.*, "All-Epitaxial Integration of Long-Wavelength Infrared Plasmonic Materials and Detectors for Enhanced Responsivity," ACS Photonics **7**(8), 1950–1956 (2020).
30. A. Kamboj, L. Nordin, P. Petluru, *et al.*, "All-epitaxial guided-mode resonance mid-wave infrared detectors," Appl. Phys. Lett. **118**(20), 201102 (2021).
31. L. Nordin, P. Petluru, A. Kamboj, *et al.*, "Ultra-thin plasmonic detectors," Optica **8**(12), 1545 (2021).
32. L. Nordin, A. J. Muhowski, and D. Wasserman, "High operating temperature plasmonic infrared detectors," Appl. Phys. Lett. **120**(10), 101103 (2022).
33. L. Nordin and D. Wasserman, "Epitaxial mid-IR nanophotonic optoelectronics," Appl. Phys. Lett. **120**(22), 220501 (2022).
34. A. Kamboj, L. Nordin, A. J. Muhowski, *et al.*, "Room-Temperature Mid-Wave Infrared Guided-Mode Resonance Detectors," IEEE Photonics Technol. Lett. **34**(11), 615–618 (2022).
35. P. Petluru, A. J. Muhowski, A. Kamboj, *et al.*, "All-epitaxial resonant cavity enhanced long-wave infrared detectors for focal plane arrays," Appl. Phys. Lett. **122**(2), 021101 (2023).
36. P. Klipstein, Y. Benny, S. Gliksman, *et al.*, "Minority carrier lifetime and diffusion length in type II superlattice barrier devices," Infrared Phys. Technol. **96**, 155–162 (2019).
37. X. Li, D. Jiang, Y. Zhang, *et al.*, "Investigations of quantum efficiency in type-II InAs/GaSb very long wavelength infrared superlattice detectors," Superlattices Microstruct. **92**, 330–336 (2016).
38. E. Giard, I. Ribet-Mohamed, M. Delmas, *et al.*, "Influence of the p-type doping on the radiometric performances of MWIR InAs/GaSb superlattice photodiodes," Infrared Phys. Technol. **70**, 103–106 (2015).
39. C. Maës, G. Vincent, F. González-Posada Flores, *et al.*, "Semiconductor-based nanostructures for spectral filtering," in *Plasmonics: Design, Materials, Fabrication, Characterization, and Applications XVII*, T. Tanaka and D. P. Tsai, eds. (SPIE, San Diego, United States, 2019), p. 68.
40. T. Taliercio, V. N. Guilengui, L. Cerutti, *et al.*, "Brewster mode in highly doped semiconductor layers: an all-optical technique to monitor doping concentration," Opt. Express **22**(20), 24294–24303 (2014).
41. S. Adachi, "Optical dispersion relations for GaP, GaAs, GaSb, InP, InAs, InSb, AlxGa1-xAs, and In1-xGaxAsyP1-y," J. Appl. Phys. **66**(12), 6030–6040 (1989).
42. P.-F. Qiao, S. Mou, and S. L. Chuang, "Electronic band structures and optical properties of type-II superlattice photodetectors with interfacial effect," Opt. Express **20**(3), 2319 (2012).
43. E. Steveler, M. Verdun, B. Portier, *et al.*, "Optical index measurement of InAs/GaSb type-II superlattice for mid-infrared photodetection at cryogenic temperatures," Appl. Phys. Lett. **105**(14), 141103 (2014).
44. N. Gautam, A. Barve, and S. Krishna, "Identification of quantum confined interband transitions in type-II InAs/GaSb superlattices using polarization sensitive photocurrent spectroscopy," Appl. Phys. Lett. **101**(22), 221119 (2012).
45. E. Sakat, G. Vincent, P. Ghenuche, *et al.*, "Guided mode resonance in subwavelength metallodielectric free-standing grating for bandpass filtering," Opt. Lett. **36**(16), 3054–3056 (2011).
46. 'https://recherche.data.gouv.fr,' https://doi.org/10.57745/PZSHNZ.

144.204.16.1 {ts '2024-05-08 03:30:57'}